LJMU Research Online

He, Y, Wang, J, Zhu, T, Ren, X, Guo, J and Yang, Q

 Insights into refinement mechanism of primary M7C3 carbide by La2O3 via experiments and first-principles calculations

https://researchonline.ljmu.ac.uk/id/eprint/22841/

Article

For more information please contact researchonline@ljmu.ac.uk

Insights into refinement mechanism of primary M_7C_3 carbide by La_2O_3 via experiments and first-principles calculations

Yuenian He [a], Jibo Wang [b,**], Tianfang Zhu [a], Xuejun Ren [c], Jing Guo [d], Qingxiang Yang [a,*]

[a] State Key Laboratory of Metastable Materials Science & Technology, Hebei Key Lab for Optimizing Metal Product Technology and Performance, Yanshan University, Qinhuangdao, 066004, PR China
[b] Fujian Provincial Key Laboratory of Welding Quality Intelligent Evaluation, Longyan University, Longyan, 364012, PR China
[c] School of Engineering, Liverpool John Moores University, Liverpool, L3 3AF, UK
[d] Henry Royce Institute for Advanced Materials, The University of Manchester, Manchester, M19 3PL, UK

ABSTRACT

This study is dedicated to summarize refinement mechanism of the primary M_7C_3 carbide by rare earth oxide La_2O_3. The La_2O_3 was added into hypereutectic Fe–27Cr–4C alloy, and its microstructure was observed and analyzed by optical microscope (OM), X-ray diffractometer (XRD) and scanning electron microscope (SEM). The lattice mismatch degrees of $La_2O_3//M_7C_3$ interfaces were calculated. The interface properties of $La_2O_3//M_7C_3$ were calculated by the first principles. The effectiveness of La_2O_3 as the heterogeneous nucleus of the primary M_7C_3 carbide in the alloy was analyzed. The results show that the primary M_7C_3 carbide can be refined by La_2O_3 in this alloy. The lattice mismatch degree between $La_2O_3(111)$ plane and $M_7C_3(0001)$ plane is 2.36%, which indicates that La_2O_3 as the heterogeneous nucleus of M_7C_3 is the most effective. $La_2O_3(111)$ plane and $M_7C_3(0001)$ plane were chosen to construct the interface models. Two surface models, such as La-termination and O1-termination on $La_2O_3(111)$ plane were constructed, which converge to 26 and 21 layers, and their surface energies are 5.256 J/m^2 and 2.029 J/m^2, respectively. The surface model of $M_7C_3(0001)$ plane converges to 17 layers, and its surface energy is 3.199 J/m^2. Among La-M_7C_3 and O1-M_7C_3 interfaces, the adhesion work (16.162 J/m^2) of O1-M_7C_3 is larger than that (1.731 J/m^2) of La-M_7C_3. However, the interface energy (-10.910 J/m^2) of O1-M_7C_3 is smaller than that (6.725 J/m^2) of La-M_7C_3, which indicates that O1-M_7C_3 interface has the best interface bonding property and the lowest interface nucleation resistance. Therefore, La_2O_3 can serve as the heterogeneous nucleus of M_7C_3 and tends to form an O1-M_7C_3 heterogeneous nucleation interface.

1. Introduction

Hypereutectic Fe–Cr–C alloy coating has excellent wear resistance, which has been widely applied in additive manufacturing industry [1,2]. The primary M_7C_3 carbide is the strengthening phase of the coating. The service life of the workpieces manufactured by the hypereutectic Fe–Cr–C alloy is determined by large number of the dispersed primary M_7C_3 carbide [3,4]. During the solidification process, the primary M_7C_3 carbides precipitine directly from the liquid metal and grow rapidly. Until the eutectic reaction occurs, the precipitation process of the primary M_7C_3 carbide ends, which exist with large size and polygon in the eutectic matrix [5]. During the service of the workpieces manufactured by this coating, the primary M_7C_3 carbides tend to peel off from the

surface of the workpieces, so as to reduce its service life [6,7]. Therefore, it is the significant to refine the primary M_7C_3 carbide for improving the service performance of the hypereutectic Fe–Cr–C alloy coating.

In recent years, with its high melting point and stability, the typical rare earth oxide La_2O_3 has been directly applied into various alloys to improve the microstructure and enhance the mechanical property, corrosion resistance and wear resistance [8,9]. Chen et al. [10] investigated the addition of La_2O_3 on grain refinement of additive manufactured Ti-6.5Al-3.5Mo-1.5Zr-0.3Si titanium alloy. The results show that the La_2O_3 can significantly refine the prior β grains. Zhou et al. [11] analyzed the effect of La_2O_3 addition on microstructure and mechanical properties of TiC-based cermets. It can been see that the toughness and density are increased as a result of the well-developed grey rims around

---

the black cores and the wettability between the ceramic and metallic phases is improved. Qu et al. [12] studied the corrosion and wear properties of TB2 titanium alloy borided by pack boriding with La_2O_3. It was found that the wear and corrosion resistances of TB2 alloy are enhanced by boriding with La_2O_3.

Currently, it is intriguing to add La_2O_3 into the hypereutectic Fe–Cr–C alloy coating to refine the primary M_7C_3 carbide. Yang et al. [13] studied the microstructure and wear resistance of the hypereutectic Fe–Cr–C alloy coating with different La_2O_3 additives. It was found that with the increase of the La_2O_3 addition, the dimension of the primary M_7C_3 carbide in the coating is decreased gradually and its wear resistance is increased firstly then decreased and reaches the most excellent when the La_2O_3 addition is 0.78 wt%. However, the mechanism of the primary M_7C_3 carbide was refined by La_2O_3 in this coating has not been reported. Moreover, it is difficult to determine the interfacial properties between La_2O_3 and M_7C_3 carbide by experimental method, so as to reveal whether La_2O_3 can be as the heterogeneous nucleus of the primary M_7C_3 carbide.

At present, the first principles methods have been widely applied to study the surface and interface for different material, and explain the bonding characteristics among atoms from the electronic structure [14, 15]. Jiao et al. [16] calculated on the γ-Fe/La_2O_3 interface properties by first-principles and analyzed the austenite refinement mechanism by La_2O_3. Lu et al. [17] studied the influence of solute elements (Cr, Mo, Fe, Co) on the binding properties of WC/Ni interface by using the first-principles method, and found that element Mo would reduce the binding strength of WC/NiMo interface, while the addition of elements Cr and Mo would enhance the binding strength of the interface. Therefore, it is feasible to investigate the interfacial structure and bonding strength between La_2O_3 and M_7C_3 carbide at atomic scale by first principles calculation, and explain the mechanism of the primary M_7C_3 carbide refined by La_2O_3.

In this paper, the microstructure of the hypereutectic Fe–27Cr–4C alloy coating with La_2O_3 was observed and analyzed by optical microscope (OM), X-ray diffractometer (XRD) and scanning electron microscope (SEM). The lattice mismatch degrees of La_2O_3//M_7C_3 interfaces were calculated. The interface properties of La_2O_3//M_7C_3 interfaces were also calculated by the first principles. The effectiveness of La_2O_3 as the heterogeneous nucleus of the primary M_7C_3 carbide in hypereutectic Fe–Cr–C alloy coating was analyzed.

2. Experimental materials and method

2.1. Experimental materials

In this paper, the hypereutectic Fe–27Cr–4C alloy coating was designed and prepared by adding La_2O_3, and the additions of La_2O_3 were 0 wt% and 0.80 wt%, respectively. Firstly, Axiovert 200 MAT optical microscope (OM), Hitachi S4800 field emission scanning electron microscope (FESEM) with energy dispersive spectrometer (EDS) were used to visualize the microstructure and carbide morphology of the coatings. Then, the phase structure and orientation of the coatings were determined by D/Max-2500/PC X-ray diffractometer (XRD). The coating specimens were smoothed and polished before testing to ensure the reliability of the test data. The X-ray source was Cu-Ka target, the range of measurement angle was 20–120°, and the measurement step was 2°/min. The morphology, size and distribution of the carbide in the coatings were quantitatively analyzed by Image-Pro Plus software. Finally, the Talos F200X transmission electron microscope (TEM) was used to observe the crystal structure of the coatings. Model691 precision argon ion thinning instrument (Model691 PIPS) was applied in the ion thinning process for coating specimen preparation.

2.2. Computational details

In this paper, the Vienna Ab Initio Simulation Package (VASP) [18]

based on density functional theory was used to optimize the bulk phase structure of M_7C_3 and La_2O_3, and their surface and interface properties were calculated. The generalized gradient approximation (GGA) functional modified by Perdew, Burke and Ernzerhof (PBE) was used to calculate and correct the exchange correlation energy [19]. Projection augmented wave (PAW) was used to describe the interaction between ionic nuclei and valence electrons [20]. The suitable plane wave cutoff energy (E_{cut}) and Brillouin K-point grid (K_{mesh}) are selected by convergence test, and the convergence test criteria were as follows. The energy change value was less than 1×10^{-5} eV/atom, the maximum force acting on each atom was less than 0.02 eV/Å, and the maximum displacement was less than 1.0×10^{-3} Å. Therefore, E_{cut} was set as 500 eV, and K_{mesh} was set as $5 \times 5 \times 5$ in the optimization of the bulk structure of M_7C_3. When the La_2O_3 bulk structure was optimized, the E_{cut} was 400 eV and the K_{mesh} was $8 \times 8 \times 8$. When the surface properties of M_7C_3 was calculated, E_{cut} was selected as 500 eV and K_{mesh} was $5 \times 5 \times 1$, which is same as the experimental value [21]. When the interface properties of La_2O_3 were calculated, E_{cut} was selected as 500 eV and K_{mesh} was $5 \times 5 \times 1$, which is same as the experimental value [22]. Finally, when their interface properties were calculated, the E_{cut} was selected as 500 eV and the K_{mesh} was $5 \times 5 \times 1$.

3. Experimental characterization

3.1. Effect of La_2O_3 on size of the primary M_7C_3 carbide

The microstructures of the hypereutectic Fe–Cr–C alloy coating with and without La_2O_3 are shown in Fig. 1.

Fig. 1(a) is that of the coating with 0.80 wt% addition of La_2O_3. It can be seen that the primary M_7C_3 carbides present irregular polygonal distribution. According to the carbide size statistics, the average size of the primary M_7C_3 carbides in the coating with La_2O_3 is 25 μm. The size change of the primary M_7C_3 carbide is not obvious, and the primary M_7C_3 carbide are distributed uniformly. Fig. 1(b) is that of the coating without La_2O_3. It can be clearly seen that its average size is 28 μm, and they are not distributed uniformly.

3.2. Nucleation analysis

3.2.1. FESEM analysis

The FESEM of the primary M_7C_3 carbide with La_2O_3 is shown in Fig. 2. It can be clearly seen that there is obvious bright spot on the surface of the polygon and large block primary M_7C_3 carbide, which is marked as EDS Spot 1 in Fig. 2, and EDS analysis results are listed in Table 1. From Table 1, a certain amount of element La is detected in the bright spot, which indicates that when La_2O_3 is added into the hypereutectic Fe–Cr–C alloy coating, La_2O_3 maybe the heterogeneous nucleus of the primary M_7C_3 carbide, which can be refined.

The random spot marked as Selected Area 1 on the surface of the primary M_7C_3 carbide is shown in Fig. 2, too, and the approximate atomic ratio of the primary M_7C_3 carbide can be obtained by EDS analysis, as listed in Table 2. It can be seen that the atomic number ratio of the elements Fe, Cr and C accords with the relationship of 3:4:3, which means that the primary M_7C_3 carbide is $Fe_3Cr_4C_3$ one. Zhang et al. [23] calculated the formation energy of various M_7C_3 carbide composed with different Fe and Cr atomic proportions, and found that the formation energy of $Fe_3Cr_4C_3$ is the lowest, which indicates that it is the most stable. According to the analysis of the experimental results, it is found that the atomic composition of the primary M_7C_3 carbide is consistent with the proportion of $Fe_3Cr_4C_3$. Therefore, the structure of $Fe_3Cr_4C_3$ is adopted in the subsequent calculation to simulate that of M_7C_3 carbide in this paper.

3.2.2. TEM observation

The TEM bright field image of the coating with La_2O_3 is shown in Fig. 3. It can be clearly seen that the region A with significantly different
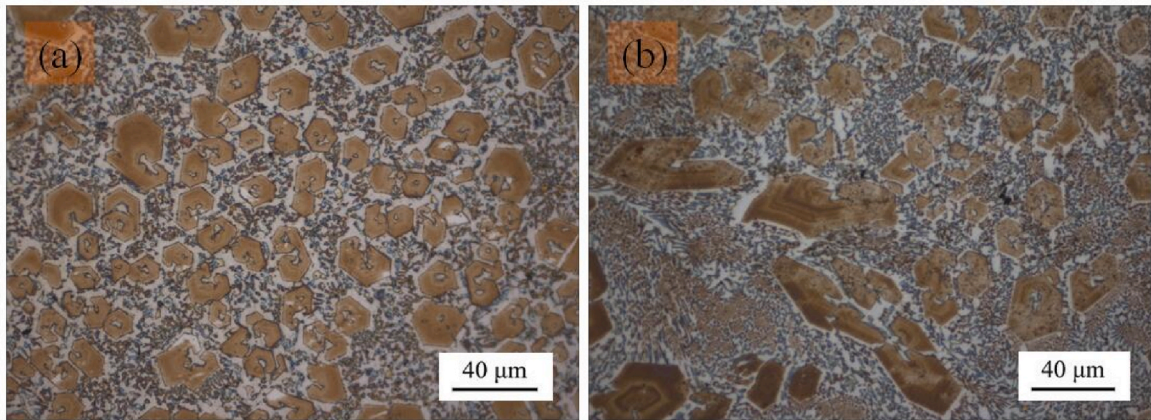
Fig. 1. Microstructures of hypereutectic Fe–Cr–C alloy coating with and without La$_2$O$_3$. (a) 0.80 wt%; (b) 0 wt%.
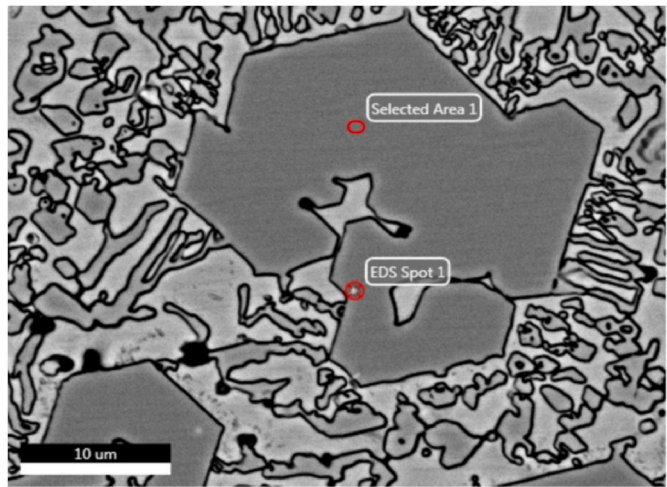

Fig. 2. FESEM of the primary M$_7$C$_3$ carbide with La$_2$O$_3$.

Table 1
Proportion of elements contained in EDS Spot 1.

Element	Fe	Cr	C	La
Proportion (at.%)	20.98	24.08	32.98	4.70

Table 2
Proportion of elements contained in Selected Area 1.

Element	Fe	Cr	C
Proportion (at.%)	29.05	43.16	27.79

contrast and the region B growing around the region A.

In order to distinguish the element composition of each region, a face scan was performed on Fig. 3, which is shown in Fig. 4.

Fig. 4(a)–(d) are the distributions of the elements C, Cr, Fe and La, respectively. It can be clearly seen that region A and region B are dependent on each other. The elements C, Cr and Fe mainly gather in the region B, while the element La obviously gather in the region A.

In order to determine the species and crystal structure of the region A and region B, the diffraction spots were collected and calibrated, as shown in Fig. 5. Fig. 5(a) is the diffraction pattern of region A, the crystal plane spacing of (010), (100) and (110) are equal to 3.42 Å, which is generated by the diffraction of the [001] zone axis. The PDF card
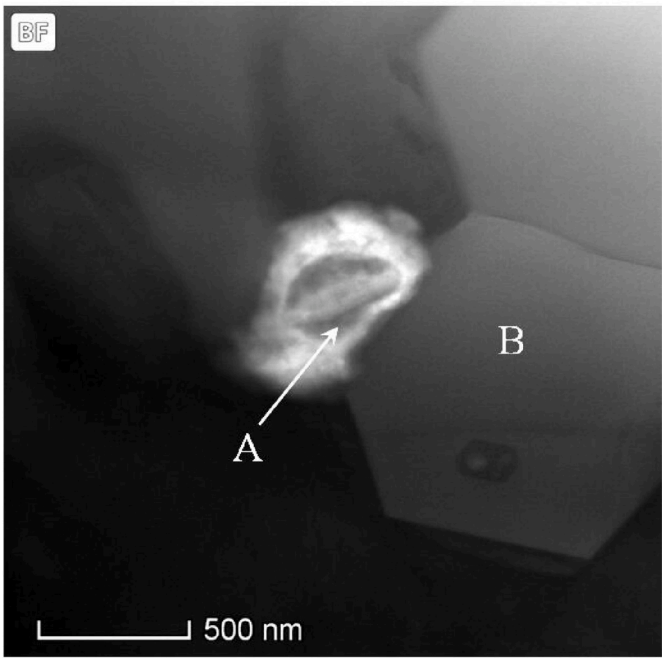

Fig. 3. TEM bright field image of the coating with La$_2$O$_3$.

information was found in Jade 6, and compared with the diffraction pattern in Fig. 5(a). It is determined to be La$_2$O$_3$ and the space group is P-3m1 (164). Fig. 5(b) is the diffraction pattern of region B, the crystal plane spacing of (1$\bar{1}$00), (10$\bar{1}$0) and (01$\bar{1}$0) are 6.05 Å, which is generated by the diffraction of the [0001] zone axis. Since the structure of M$_7$C$_3$ is obtained by Cr atoms replacing part of Fe atoms in Fe$_7$C$_3$, it is found from the PDF card of Jade 6 that the crystal plane spacing of Fe$_7$C$_3$ and Cr$_7$C$_3$ is 5.96 Å and 6.07 Å respectively, which is similar to the results in Fig, 5(b). Therefore, it is determined to be M$_7$C$_3$ and its space group is P63mc (186).

4. Lattice mismatch degree between La$_2$O$_3$ and M$_7$C$_3$

According to Bramfitt two-dimensional lattice mismatch theory [24], the lattice mismatch degree between M$_7$C$_3$ and La$_2$O$_3$ must meet the following requirements: La$_2$O$_3$ cannot be used as the heterogeneous nucleation nucleus when the mismatch degree is larger than 12%, while when the mismatch degree is between 6% and 12%, it belongs to the range of medium effective nucleation, and when the mismatch degree is
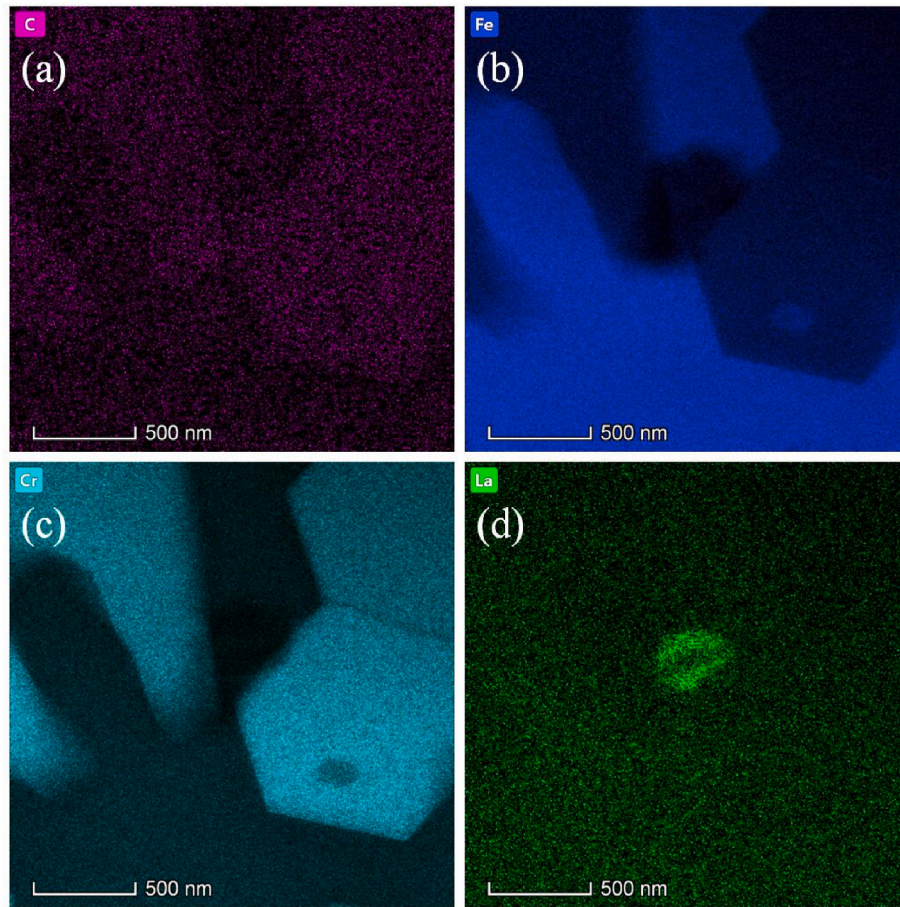
Fig. 4. Element mapping images of the M_7C_3 carbide with La_2O_3. (a) C; (b) Fe; (c) Cr; (d) La.
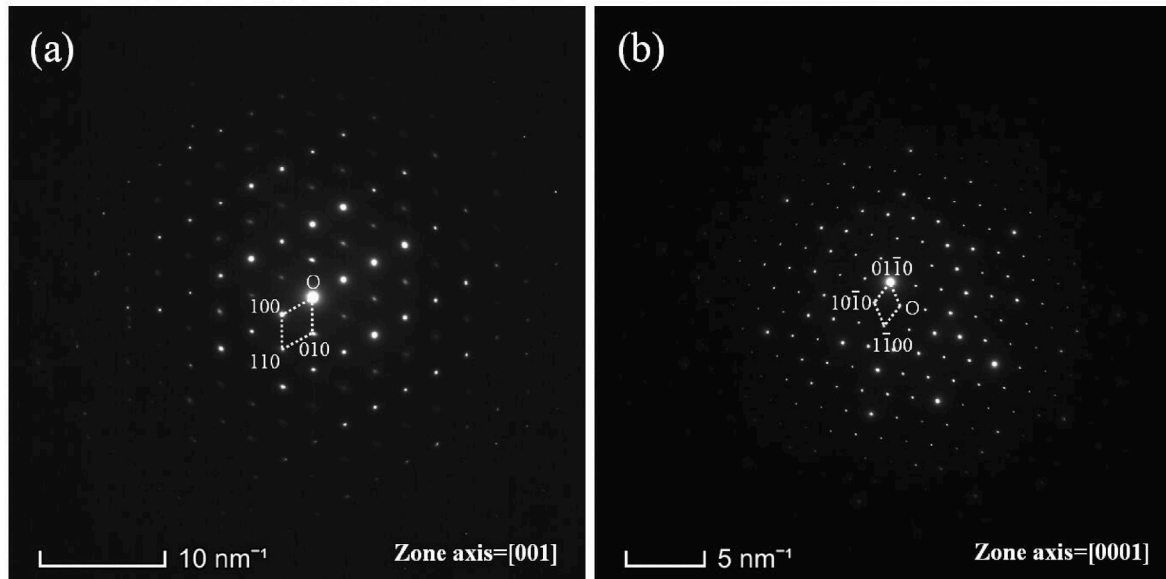

Fig. 5. Diffraction spot images of region A and region B. (a) Region A; (b) Region B.

within 6%, it belongs to the range of effective nucleation. The formula of two-dimensional lattice mismatch degree is as follows [24].

$$\delta_{(hkl)_n}^{(hkl)_s} = \sum_{i=1}^{3} \left[\left(\left| d_{[uvw]_s}{}^i \cos\theta - d_{[uvw]_n}{}^i \right| / d_{[uvw]_n}{}^i \right) / 3 \right] \times 100\% \qquad (1)$$

where $(hkl)_s$ is a low-index plane of the matrix; $[uvw]_s$ is a low-index direction on $(hkl)_s$; $d_{[uvw]s}$ is the atomic spacing along the $[uvw]_s$ direction; $(hkl)_n$ is a low-index plane of the crystalline phase; $[uvw]_n$ is a low-index direction on $(hkl)_n$; $d_{[uvw]n}$ is the atomic spacing along the $[uvw]_n$ direction; θ is the angle between the $[uvw]_s$ and $[uvw]_n$; i is the

value of the three low-index directions on the three low-index planes of the crystal phase.

The lattice mismatch degrees between M_7C_3 and La_2O_3 are listed in Table 3. It can be seen that the lattice mismatch degree between M_7C_3 (0001) plane and La_2O_3 (111) plane is 2.36%, which is the most effective heterogeneous nucleation one. Therefore, M_7C_3 (0001) plane and La_2O_3 (111) plane are chosen to construct coherent interface models.

5. Nucleation interface analysis

5.1. Crystal structure and bulk phase properties of La₂O₃ and M₇C₃

The crystal structures of La_2O_3 and M_7C_3 are shown in Fig. 6. Fig. 6 (a) is the crystal structure of La_2O_3, whose optimized lattice constants are a = b = 3.93 Å and c = 6.12 Å. Fig. 6(b) is that of M_7C_3, whose optimized lattice constants are a = b = 6.98 Å and c = 4.27 Å.

The calculated band structure and density of state of La_2O_3 are shown in Fig. 7. Among them, Fig. 7(a) is the band structure of La_2O_3, and the red dashed line is the Fermi level. It can be clearly seen that the energy band of La_2O_3 does not pass through the Fermi level, while there is a certain band gap between the valence band and the conduction band, and its band gap energy is 3.86 eV, which indicates that it embodies certain semiconductor properties. Fig. 7(b) is the density of state of La_2O_3. It can be clearly seen that the O-s orbital resonates with the La-p orbital, which indicates there is a covalent bond between them. The gravity center of orbital state density between La-d and O-p orbitals is inconsistent, which indicates that there is a strong ionic bond. It can be seen that covalent and ionic bonds are exist at the La_2O_3 phase structure.

The calculated band structure and density of state of M_7C_3 are shown in Fig. 8. Among them, Fig. 8(a) is the band structure of M_7C_3. It can be seen that there are energy bands passing through the Fermi level, and electrons in the valence band can easily transition to the conduction band, which indicates that M_7C_3 has metallic properties. Fig. 8(b) is the density of state of M_7C_3. The presence of electrons at the Fermi level is consistent with the band structure and reflects the metallic properties of M_7C_3, which has metallic bonds within it. It can be found that the similar waveforms at −7.5 to −4.3 eV appear among the Fe-d, Cr-d and C-p orbitals, and they all contribute to the density of states, which indicates that there are covalent bonds between them. However, the gravity center of the orbital state density between Fe-d, Cr-d and C-p orbitals are inconsistent, which indicates that there is an ionic bond. It can be seen that metallic, covalent and ionic bonds are exist at the M_7C_3 phase structure.

5.2. Surfaces convergence of La₂O₃ and M₇C₃

According to the lattice mismatch degrees between M_7C_3 and La_2O_3 in Table 3. M_7C_3 (0001) plane and La_2O_3 (111) plane are selected to construct coherent interface model.

The surface models of La_2O_3 (111) plane and M_7C_3 (0001) plane are shown in Fig. 9. La_2O_3 (111) plane is a polar surface. In the surface model construction of La_2O_3 (111) plane, the difference in the starting position of the cut layer will lead to the difference in the atomic type of the end surface. Therefore, the surface models of three different termination ones for La_2O_3 (111) plane can be obtained, namely, O1-Terminated, La-Terminated, and O2-Terminated models, as shown in Fig. 9(a)–(c). The surface model of M_7C_3 (0001) plane is shown in Fig. 9 (d).

The surface energy converges gradually with the increase of atomic

Table 3
Calculated lattice mismatch degrees between M_7C_3 and La_2O_3.

Matching plane	M_7C_3(0001)// La_2O_3(111)	M_7C_3(0001)// La_2O_3(001)	M_7C_3(0001)// La_2O_3(110)
δ (%)	2.36	12.38	17.60

layers number. Botteger formula [25] was used to calculate the surface energy of La_2O_3 (111) and M_7C_3 (0001) planes.

The surface energy formula of La_2O_3 (111) plane is as follows:

$$\sigma_{La2O3(111)} = \frac{1}{2A}[E_{slab} - N_{La}\mu_{La} - N_O\mu_O] \quad (2)$$

where $\sigma_{La2O3(111)}$ is the surface energy of La_2O_3 (111) plane; A is the surface area of La_2O_3 (111) plane; E_{slab} is the total energy of La_2O_3 (111) plane; N_{La} and N_O are the number of La atoms and O atoms of La_2O_3 (111) plane, respectively; μ_{La} and μ_O are the chemical potential of La atoms and O atoms, respectively.

For La_2O_3 phase structure, the formula is as follows:

$$\mu_{La2O3}^{bulk} = 3\mu_O + 2\mu_{La} \quad (3)$$

where μ_{La2O3}^{bulk} is the energy of La_2O_3 phase structure.

Combining Eqs. (2) and (3), the surface energy of La_2O_3 (111) plane is obtained as follows:

$$\sigma_{La2O3(111)} = \frac{1}{2A}\left[E_{slab} - \frac{1}{2}N_{La}\mu_{La2O3}^{bulk} + \left(\frac{3}{2}N_{La} - N_O\right)\mu_O\right] \quad (4)$$

The calculated surface energies of La_2O_3 (111) plane are listed in Table 4. It can be seen that the O1-Terminated model converges to 21 layers, and its surface energy is 2.029 J/m². The La-Terminated model converges to 26 layers, and its surface energy is 5.256 J/m². The O2-Terminated model can never converge within this range, which indicates that the surface of the terminated model is not stable within this range of layers.

The surface energy of M_7C_3 (0001) plane can be expressed as follows:

$$\sigma_{M_7C_3(0001)} = \frac{1}{2A}[E_{slab} - N_{Fe}\mu_{Fe} - N_{Cr}\mu_{Cr} - N_C\mu_C] \quad (5)$$

where $\sigma_{M7C3(0001)}$ is the surface energy of M_7C_3 (0001) plane; A is the surface area of M_7C_3 (0001) plane; E_{slab} is the total energy of M_7C_3 (0001) plane; N_{Cr}, N_C and N_{Fe} are the numbers of Cr, C and Fe atoms of M_7C_3 (0001) plane, respectively; μ_{Cr}, μ_C and μ_{Fe} are the chemical potential of Cr, C and Fe atoms, respectively.

For M_7C_3 phase structure, the formula is as follows:

$$\mu_{M_7C_3}^{bulk} = 3\mu_{Fe} + 4\mu_{Cr} + 3\mu_C \quad (6)$$

In the surface model of M_7C_3 (0001) plane constructed by cell superposition, the formula can be expressed as follows:

$$N_{Fe} = N_C = \frac{3}{4}N_{Cr} \quad (7)$$

Combining Eqs. (5)–(7), the surface energy of M_7C_3 (0001) plane is obtained as follows:

$$\sigma_{M_7C_3(0001)} = \frac{1}{2A}\left[E_{slab} - \frac{N_{Cr}}{8}\mu_{Fe_3Cr_4C_3}^{bulk} + \left(\frac{3}{4}N_{Cr} - N_{Fe}\right)\mu_{Fe}\right] \quad (8)$$

The calculated surface energies of M_7C_3 (0001) plane are listed in Table 5. It can be seen that the surface model of M_7C_3 (0001) plane converges to 17 layers, and its surface energy is 3.199 J/m².

5.3. Interface properties of La₂O₃//M₇C₃

5.3.1. Interface structure

From the above calculation results, it can be seen that the surface model of M_7C_3 (0001) plane converges to 17 layers, and those of La-termination and O1-termination surface models of La_2O_3 (111) plane converge to 26 layers and 21 layers, respectively. Therefore, the 26 layer La-termination and 21 layer O1-termination surface models of the La_2O_3 (111) planes are used to construct interface models with 17 layers model of M_7C_3 (0001) plane, and they are named as La-M_7C_3 interface and O1-M_7C_3 interface, respectively, which are shown in Fig. 10. The dashed
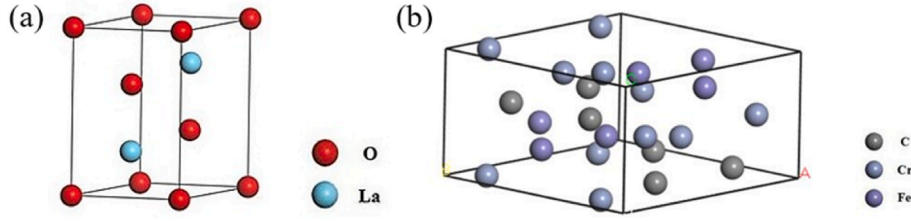
Fig. 6. Crystal structures of La$_2$O$_3$ and M$_7$C$_3$. (a) La$_2$O$_3$; (b) M$_7$C$_3$.
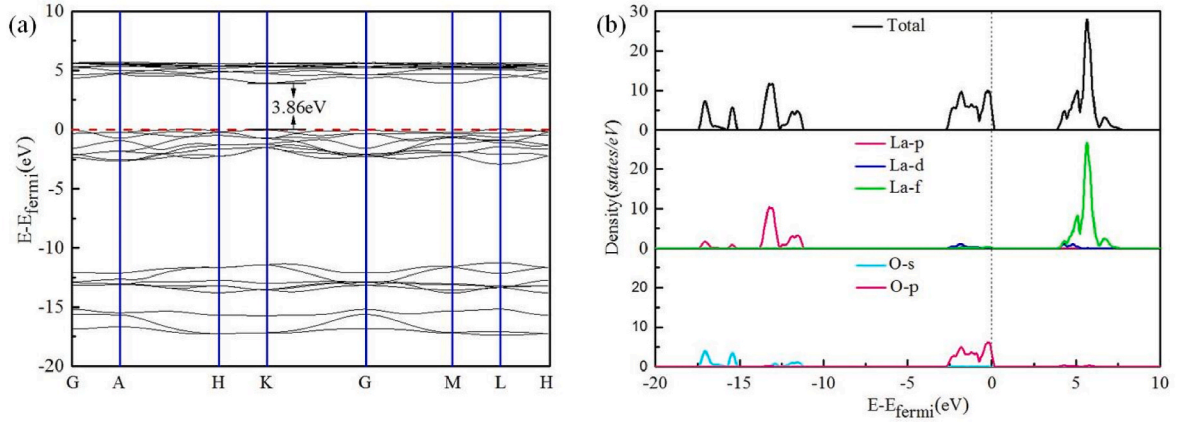

Fig. 7. Band structure and density of states of La$_2$O$_3$. (a) Band structure; (b) Density of states.
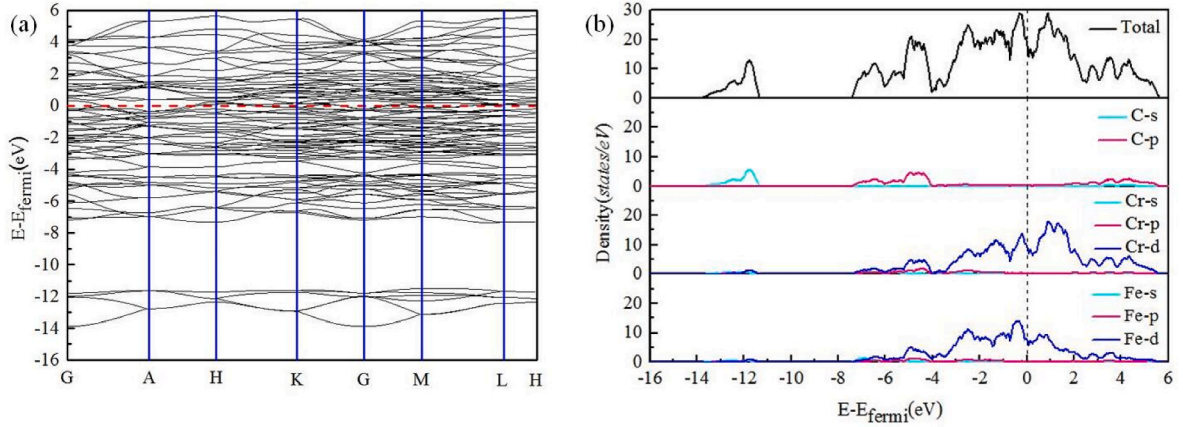

Fig. 8. Band structure and density of states of M$_7$C$_3$. (a) Band structure; (b) Density of states.

lines are the interface positions.

5.3.2. Interfacial stability

Adhesion work (W_{ad}) of an ideal interface is the reversible work done to separate an interface into two free surfaces per unit area. The higher the interfacial bonding work is, the higher the probability of interfacial formation is, and the stronger the interatomic bonding at the interface is.

The W_{ad} of M$_7$C$_3$(0001)//La$_2$O$_3$(111) interface can be calculated by the following equation [26].

$$W_{ad} = \frac{1}{A}\left(E_{La_2O_3} + E_{M_7C_3} - E_{La_2O_3//M_7C_3}\right) \tag{9}$$

where W_{ad} is the adhesion work of interface; A is the interface area; $E_{M_7C_3}$ and $E_{La_2O_3}$ are the total energy of the M$_7$C$_3$ (0001) plane and La$_2$O$_3$ (111) plane, respectively; $E_{La_2O_3//M_7C_3}$ is the total energy of the interface model.

The W_{ad} of La-M$_7$C$_3$ and O1-M$_7$C$_3$ interfaces were calculated, and the results are listed in Table 6. It can be seen that the W_{ad} (16.162 J/m^2) of O1- M$_7$C$_3$ interface is much larger than that (1.731 J/m^2) of La-M$_7$C$_3$ interface, which indicates that the O1-M$_7$C$_3$ interface provides the strongest interface combination capability.

Interfacial energy (γ) is another criterion to evaluate the stability of the interface. The smaller the interface is, the higher the probability of the interface formation is, and the more stable it is.

The γ of M$_7$C$_3$(0001)//La$_2$O$_3$(111) interfaces can be calculated by the following equation [27].

$$\gamma = \sigma_{La_2O_3} + \sigma_{M_7C_3} - W_{ad} \tag{10}$$

where γ is the interfacial energy of interface; $\sigma_{M_7C_3}$ and $\sigma_{La_2O_3}$ are the surface energies of M$_7$C$_3$ (0001) plane and La$_2$O$_3$ (111) plane, respectively.

The γ of La-M$_7$C$_3$ and O1-M$_7$C$_3$ interfaces were calculated, and the
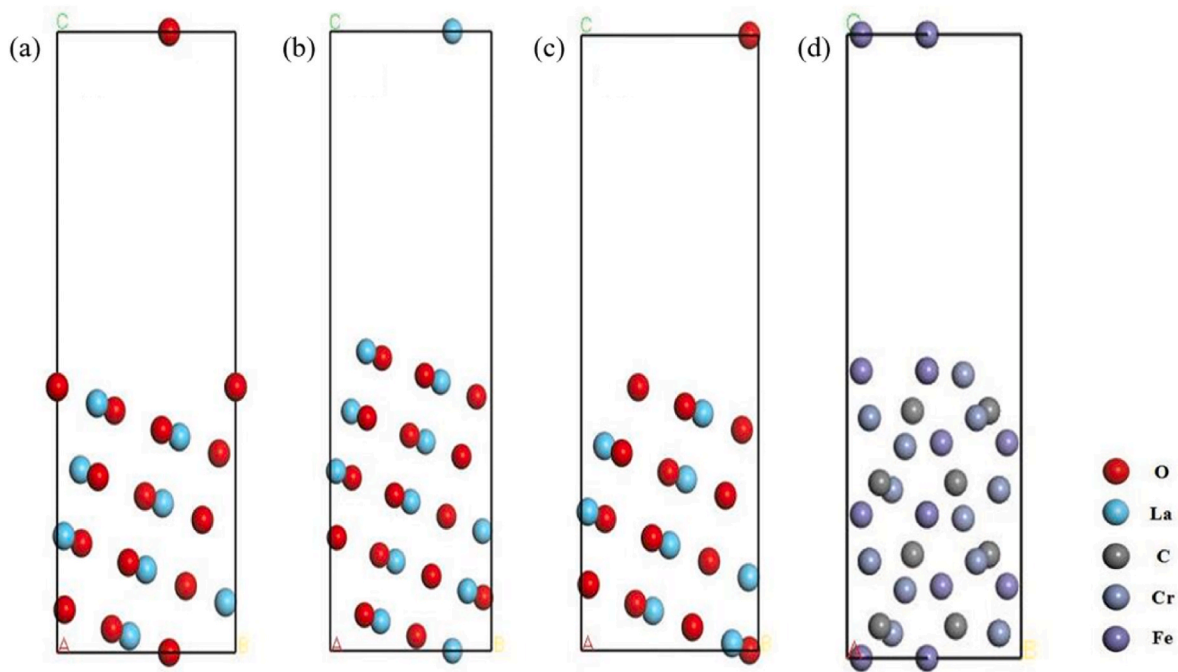
Fig. 9. Surface models of La$_2$O$_3$ (111) and M$_7$C$_3$ (0001) planes. (a) O1-Terminated; (b) La-Terminated; (c)O2-Terminated; (d) M$_7$C$_3$(0001).

Table 4
Calculated surface energies of La$_2$O$_3$(111) plane.

Layers	6	11	16	21	26	31
O1-Terminated (J/m^2)	2.017	1.820	1.861	2.029	2.053	2.088
La-Terminated (J/m^2)	4.560	4.816	5.128	5.068	5.256	5.273
O2-Terminated (J/m^2)	1.661	1.736	1.771	1.658	2.330	2.449

Table 5
Calculated surface energies of M$_7$C$_3$ (0001) plane.

Layers	9	17	25	33
M$_7$C$_3$(0001) (J/m^2)	3.132	3.199	3.209	3.229

results are listed in Table 7. It can be seen that the γ (-10.910 J/m^2) of O1-M$_7$C$_3$ interface is much smaller than that (6.725 J/m^2) of La-M$_7$C$_3$, which indicates that the O1-M$_7$C$_3$ interface provides the lowest nucleation resistance.

5.3.3. Interface electronic structure

Charge density and differential charge density were used to analyze the charge density at the interface and the bonding mechanism between atoms. Among them, the differential charge density is calculated as follows [27].

$$\rho_d = \rho_{tot} - \rho_{La_2O_3} - \rho_{M_7C_3} \tag{11}$$

where ρ_{tot} is the total charge density of the interface models; $\rho_{La_2O_3}$ and $\rho_{M_7C_3}$ are the charge density of separate La$_2$O$_3$ (111) plane and M$_7$C$_3$ (0001) plane in the same interface models.

The charge densities of M$_7$C$_3$(0001)//La$_2$O$_3$(111) interface are shown in Fig. 11, and the dotted lines represent the interface position. As shown on the right side of the scale, the charge density gradually rises from blue to red, and the positions of each atom are marked by different colored spheres. Fig. 11(a) is the charge density front view of the La-M$_7$C$_3$ interface. It can be seen that the charge of the Fe atom at the top of the interface is transferred to the O atom at the bottom of the interface,
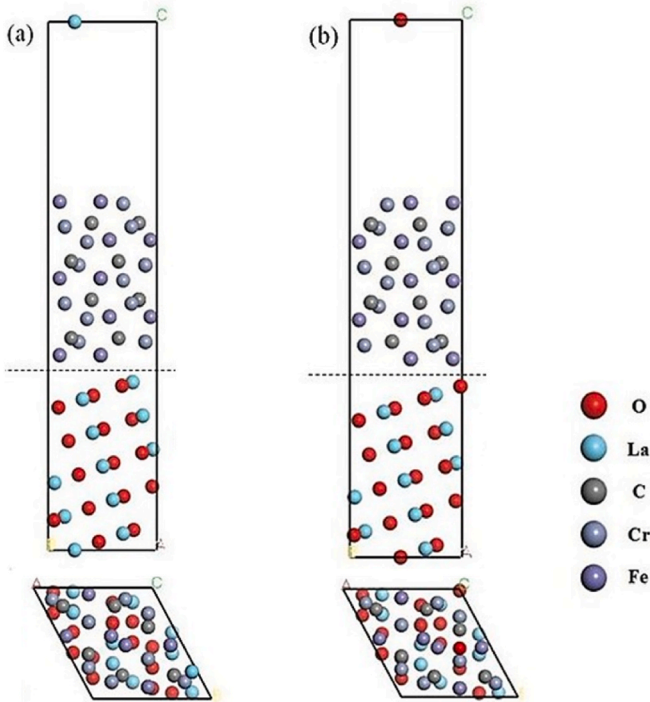

Fig. 10. Interface models of La$_2$O$_3$(111)//M$_7$C$_3$(0001) interfaces. (a) La-M$_7$C$_3$; (b) O1-M$_7$C$_3$.

Table 6
Adhesion work of M$_7$C$_3$(0001)//La$_2$O$_3$(111) interface.

	$E_{La_2O_3}$	$E_{M_7C_3}$	$E_{La_2O_3/M_7C_3}$	W_{ad}
O1-M$_7$C$_3$(J/m^2)	-10.46	-23.16	-36.71	16.162
La-M$_7$C$_3$(J/m^2)	-13.11	-23.16	-36.55	1.731

Table 7
Interfacial energy of $M_7C_3(0001)//La_2O_3(111)$ interface.

	σ_{La2O3}	σ_{M7C3}	γ
O1-M_7C_3(J/m^2)	2.053	3.199	−10.910
La-M_7C_3(J/m^2)	5.256	3.199	6.725

which indicates that there is a strong bond between the Fe atom and the O atom. Fig. 11(b) is the charge density side view of La-M_7C_3 interface. It can be seen that the charge of the C atom in the second layer above the interface also shifts significantly to the direction of O atom, which means that there is also a strong chemical bond between the C atom and the O atom. The charge of Cr atom in the fourth layer above the interface tends to shift to the lower left, which indicates that it is also affected by bonding. Therefore, it can be clearly observed that there are bonds near the interface to Fe–O, C–O, and Cr–O atoms.

Fig. 11(a') is the charge density front view of the O1-M_7C_3 interface. It can be seen that the charge of the Fe atom in the upper center of the interface is obviously transferred to the O atom below, and the Fe atom in the third layer above is also affected by the O atom below the interface directly below it, which indicates that the bonding between Fe atom and O atom is very strong. Fig. 11(b') is the charge density side view of O1-M_7C_3 interface. It can be seen that the charge of the Cr atom on the left of

the upper part of the interface is transferred to the O atom below, the charge of the Fe atom on the right is also transferred to the O atom below it, and the charge of the Cr atom above the Fe atom on the right is also transferred downward. Therefore, it can observe a large number of Fe–O and Cr–O bonds at the O1-M_7C_3 interface.

It can be seen that the charge transfer phenomenon near the interface is very obvious of two different terminating interfaces, which indicates that there are many strong bonds near the interface. Therefore, the interface bonding property of O1-M_7C_3 interface is large.

The differential charge densities of $M_7C_3(0001)//La_2O_3(111)$ interface are shown in Fig. 12, and the dotted lines represent the interface position, in which, the blue represents areas where charge is missing, red represents areas where charge is concentrated, and the positions of each atom are marked by different colored spheres. Fig. 12(a) is the differential charge density of La-M_7C_3 interface. It can be found that there are a large number of charge accumulation regions between the C atom on the left side of the interface and the O atom on the middle side of the interface, and there are obvious electron missing on the other sides of the O atom and C atoms, which indicates that a polar covalent bond is formed between C atom and O atom. However, in the upper left of this large charge accumulation region, there is Cr atom with a large loss of surrounding charges, which indicates that Cr atom and O atom formed an ionic bond. The Fe atom above the O atom in the middle of the
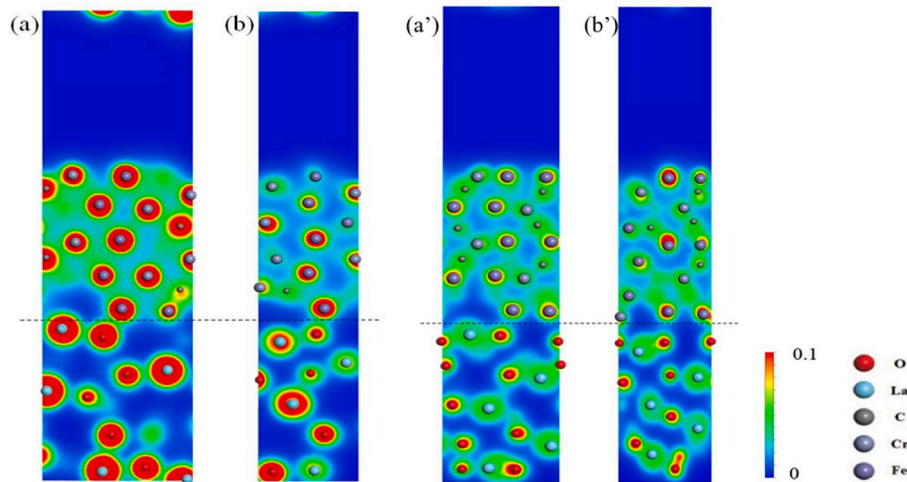

Fig. 11. Charge density of $La_2O_3(111)//M_7C_3(0001)$ interface. La-M_7C interface of (a) the front view; (b) the side view; O1-M_7C interface of (a') the front view; (b') the side view.
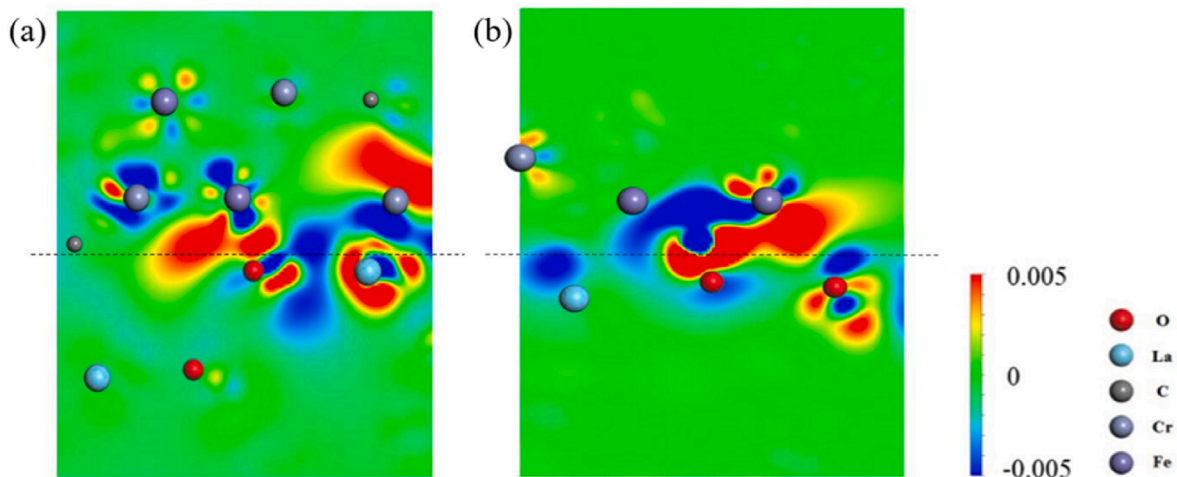

Fig. 12. Differential charge density of $La_2O_3(111)//M_7C_3(0001)$ interface. (a) La-M_7C_3; (b) O1-M_7C_3.

interface is observed, and it is found that there is also ionic bond between Fe atom and O atom. There is a charge missing region on the upper right side of Cr atom near the interface side, and the charge accumulation between the Cr atom and the C atom on the deviating interface side, which indicates that there are covalent and ionic bonds between Cr atom and C atom.

Fig. 12(b) is the differential charge density of O1-M_7C_3 interface. It shows that there is a charge accumulation area in the middle region of the interface, while there is a charge missing area around the two Fe atoms at the top, and the charge of the Fe atom at the top left is transferred to the O atom at the lower side of the interface, which indicates that it forms an ionic bond between Fe atom and O atom. The Fe atom on the right has both charge missing and charge accumulation regions around it, which indicates that it has polar covalent and ionic bonds with the two O atoms below.

6. Conclusion

(1) The hypereutectic Fe–27Cr–4C alloy coating with and without La_2O_3 was prepared. La_2O_3 can refine the primary M_7C_3 carbide in the coating, which indicates that La_2O_3 can be as the heterogeneous nucleation nucleus of the primary M_7C_3 carbide.

(2) The lattice mismatch degree between La_2O_3 (111) plane and M_7C_3 (0001) plane is 2.36%, which indicates that La_2O_3 is the most effective nucleation nucleus of primary M_7C_3 carbide.

(3) The La-terminating and O1-terminating surface models of La_2O_3 (111) plane converge to 26 layers and 21 layers respectively, whose surface energies are 5.256 J/m^2 and 2.029 J/m^2. The surface model of M_7C_3 (0001) plane converges to 17 layers, whose surface energy is 3.199 J/m^2.

(4) Among La-M_7C_3 and O1-M_7C_3 interfaces, the adhesion work (16.162 J/m^2) of O1-M_7C_3 interface is larger than that (1.731 J/m^2) of La-M_7C_3. Meanwhile, the interface energy (-10.910 J/m^2) of O1-M_7C_3 interface is smaller than that (6.725 J/m^2) of La-M_7C_3 interface, which indicates that the O1-M_7C_3 interface has the best interface bonding property and the lowest interface nucleation resistance.

Declaration of competing interest

The authors declare that they have no known competing financial interests or personal relationships that could have appeared to influence the work reported in this paper.

Acknowledgements

References

[1] Shao W, Zhou YF, Zhou L, Rao LX, Xing XL, Shi ZJ, et al. Effect of Ti-doping on peeling resistance of primary M_7C_3 carbides in hypereutectic Fes-Cr-C hardfacing coating and γ-Fe/M_7C_3 interfacial bonding strength. Mater Des 2021;211:110133. https://doi.org/10.1016/j.matdes.2021.110133.

[2] Yun X, Zhou YF, Yang J, Xing XL, Ren XJ, Yang Y, et al. Refinement of nano-Y_2O_3 on microstructure of hypereutectic Fe-Cr-C hardfacing coatings. J Rare Earths 2015;33:671–8. https://doi.org/10.1016/S1002-0721(14)60469-5.

[3] Eshed E, Choudhuri D, Osovski S. M_7C_3: the story of a misunderstood carbide. Acta Mater 2022;235:117985. https://doi.org/10.1016/j.actamat.2022.117985.

[4] Geng BY, Liu ZX, Li YK, Wang G, Zhou RF. Analysis of evolution law and mechanism of stacking fault density of M_7C_3 carbides under the action of the electric current pulse. Mater Char 2022;191:112117. https://doi.org/10.1016/j.matchar.2022.112117.

[5] Ernst F, Li DQ, Kahn H, Michal GM, Heuer AH. The carbide M_7C_3 in low-temperature-carburized austenitic stainless steel. Acta Mater 2011;59:2268–76. https://doi.org/10.1016/j.actamat.2010.11.058.

[6] Liu S, Zhang J, Wang ZJ, Shi ZJ, Zhou YF, Ren XJ, et al. Refinement and homogenization of M_7C_3 carbide in hypereutectic Fe-Cr-C coating by Y_2O_3 and TiC. Mater Char 2017;132:41–5. https://doi.org/10.1016/j.matchar.2017.08.004.

[7] Shi ZJ, Shao W, Rao LX, Hu TS, Xing XL, Zhou YF, et al. Effects of Ce doping on mechanical properties of M_7C_3 carbides in hypereutectic Fe–Cr–C hardfacing alloy. J Alloys Compd 2021;850:156656. https://doi.org/10.1016/j.jallcom.2020.156656.

[8] Zhou Q, Huang DD, Xu K, Lou M, Lv J, Wang FM, et al. Effect of La_2O_3 addition on microstructure and mechanical properties of TiC-based cermets. Ceram Int 2023; 49:18125–33. https://doi.org/10.1016/j.ceramint.2023.02.181.

[9] Yang JH, Xiao SL, Chen YY, Xu LJ, Wang XP, Zhang DD, et al. Effects of nano-Y_2O_3 addition on the microstructure evolution and tensile properties of a near-α titanium alloy. Mater Sci Eng, A 2019;761:137977. https://doi.org/10.1016/j.msea.2019.05.107.

[10] Chen YH, Yang CL, Fan CL, Zhuo YM, Lin SB, Chen C. Grain refinement of additive manufactured Ti-6.5Al-3.5Mo-1.5Zr-0.3Si titanium alloy by the addition of La_2O_3. Mater Lett 2020;275:128170. https://doi.org/10.1016/j.matlet.2020.128170.

[11] Zhou Q, Huang DD, Xu K, Lou M, Lv J, Wang FM, et al. Effect of La_2O_3 addition on microstructure and mechanical properties of TiC-based cermets. Ceram Int 2023; 49:18125–33. https://doi.org/10.1016/j.ceramint.2023.02.181.

[12] Qu DY, Liu D, Wang XY, Duan YH, Peng MJ. Corrosion and wear properties of TB2 titanium alloy borided by pack boriding with La_2O_3. T Nonferr Metal Soc 2022;32: 868–81. https://doi.org/10.1016/S1003-6326(22)65839-4.

[13] Yang J, Tian J, Hao F, Dan T, Ren XJ, Yang Y, et al. Microstructure and wear resistance of the hypereutectic Fe-Cr-C alloy hardfacing metals with different La_2O_3 additives. Appl Surf Sci 2014;289:437–44. https://doi.org/10.1016/j.apsusc.2013.10.186.

[14] Jiao XY, Fu WT, Shi ZJ, Li ZJ, Zhou YF, Xing XL, et al. First principles investigation on interface properties and formation mechanism of γ-Fe/CeO_2 heterogeneous nucleation interface. J Alloys Compd 2020;831:154867. https://doi.org/10.1016/j.jallcom.2020.154867.

[15] Mizuno M, Tanaka I, Adachi H. Chemical bonding at the Fe/TiX (X = C, N or O) interfaces. Acta Mater 1998;46:1637–45. https://doi.org/10.1016/S1359-6454(97)00344-3.

[16] Jiao XY, Fu WT, Shao W, Zhu XW, Zhou YF, Xing XL, et al. First-principles calculation on γ-Fe/La_2O_3 interface properties and austenite refinement mechanism by La_2O_3. Mater Chem Phys 2021;259:124194. https://doi.org/10.1016/j.matchemphys.2020.124194.

[17] Lu K, Shen C, He Y, Huang S, Ba Y. Effect of solute elements (Cr, Mo, Fe, Co) on the adhesion properties of WC/Ni-based binder interface: a first-principles study. Int J Refract Metals Hard Mater 2021;98:105563. https://doi.org/10.1016/j.ijrmhm.2021.105563.

[18] Kresse G, Hafner J. Ab initio molecular dynamics for liquid metals. Phys Rev B 1993;47:558–61. https://doi.org/10.1103/PhysRevB.47.558.

[19] Perdew JP, Burke K, Ernzerhof M. Generalized gradient approximation made simple. Phys Rev Lett 1997;78:1396. https://doi.org/10.1103/PhysRevLett.77.3865.

[20] Joubert D. From ultrasoft pseudopotentials to the projector augmented-wave method. Phys Rev B 1999;59:1758–75. https://doi.org/10.1103/PhysRevB.59.1758.

[21] Marco ID, Minár J, Chadov S. Correlation effects in the total energy, the bulk modulus, and the lattice constant of a transition metal: combined local-density approximation and dynamical mean-field theory applied to Ni and Mn. Phys Rev B 2009;79:111–5. https://doi.org/10.1103/PhysRevB.79.115111.

[22] Carpenter SD, Carpenter D. X-ray diffraction study of M_7C_3 carbide within a high chromium white iron. Mater Lett 2003;57:4456–9. https://doi.org/10.1016/S0167-577X(03)00342-2.

[23] Zhang PF, Zhou YF, Yang J, Li D, Ren XJ, Yang YL, et al. Optimization on mechanical properties of $Fe_{7-x}Cr_xC_3$ carbides by first-principles investigation. J Alloys Compd 2013;560:49–53. https://doi.org/10.1016/j.jallcom.2013.01.103.

[24] Bramfitt BL. The effect of carbide and nitride additions on the heterogeneous nucleation behavior of liquid iron. Metall Trans A 1970;1(7):1987–95. https://doi.org/10.1007/BF02642799.

[25] Boettger JC. Nonconvergence of surface energies obtained from thin-film calculations. Phys Rev B 1994;49:16798. https://doi.org/10.1103/PhysRevB.49.16798.

[26] Wu ZX, Pang MJ, Zhan YZ, Shu S, Xiong L, Li ZH. The bonding characteristics of the Cu (111)/WC (0001) interface: an insight from first-principle calculations. Vacuum 2021;191:110218. https://doi.org/10.1016/j.vacuum.2021.110218.

[27] Fiorentini V, Methfessel M. Extracting convergent surface energies from slab calculations. J. Phys-Condens. Mat 1996;8(36):6525. https://doi.org/10.1088/0953-8984/8/36/005.